nature physics

LETTERS

PUBLISHED ONLINE: 29 MARCH 2009 | DOI: 10.1038/NPHYS1228

Strong-field photoionization revisited

C. I. Blaga[1,2], F. Catoire[1], P. Colosimo[1], G. G. Paulus[3,4], H. G. Muller[5], P. Agostini[1] and L. F. DiMauro[1]*

Over the past thirty years, extensive studies of strong-field photoionization of atoms have revealed both quantum and classical aspects including above-threshold ionization[1], electron wave-packet drift, quiver and rescattering motions. Increasingly sophisticated spectroscopic techniques[2] and sculpted laser pulses[3] coupled with theoretical advances have led to a seemingly complete picture of this fundamental laser–atom interaction. Here, we describe an effect that seems to have escaped observation: the photoelectron energy distribution manifests an unexpected characteristic spike-like structure at low energy, which becomes prominent using mid-infrared laser wavelengths ($\lambda > 1.0\,\mu$m). The low-energy structure is observed in all atoms and molecules investigated and thus seems to be universal. The structure is qualitatively reproduced by numerical solutions of the time-dependent Schrödinger equation but its physical origin is not yet identified.

Atomic photoionization under intense laser irradiation is considered a well-understood process. In the low-intensity/short-wavelength limit, it is described quantum mechanically as multiphoton absorption: above-threshold ionization (ATI) is the absorption of photons beyond the minimum required for ionization. In the high-intensity/long-wavelength limit, the photoelectron energy distribution can be understood classically according to the Simpleman theory[4], as the drift kinetic energy of an electron as a function of the phase at which it was released in the laser cycle. Inclusion of the d.c.-tunnelling rate to describe the ionization probability completes a semi-classical theory. A corresponding quantum approach is provided by the Keldysh–Faisal–Reiss[5–7] (KFR) strong-field approximation. The KFR theory incorporates the effect of the external field on the continuum state but neglects the influence of the core potential and ignores the atom's excited states. Keldysh linked these two limits in terms of a single dimensionless parameter $\gamma = \sqrt{(IP/2U_p)}$, where IP is the ionization potential and U_p is the cycle-averaged kinetic energy of an electron quivering in the field. In the limit defined by $\gamma < 1$, the electric field of the wave can be considered quasi-static and the total ionization rate approximated by d.c.-tunnelling in accordance with the semi-classical picture. The photoelectron distribution in this case has a classical cutoff energy at $2U_p$. A more elusive feature, discovered in the mid-nineties[8,9], is the plateau in the photoelectron distribution extending to $10U_p$. Understanding the origin of this plateau requires a straightforward extension of the Simpleman theory that enables a returning electron to elastically scatter off the core. As illustrated in the inset of Fig. 1, the photoelectron spectrum exhibits both of these features, 'direct' and 'rescattered'. The amplitude of the plateau can be described by the scattering cross-section and the spread of the electron wave packet[10]. More detailed features associated with rescattering, such as the plateau's angular distributions, can be understood by the semi-classical treatment[1,10] and structural information can be retrieved from the electron momenta[11,12].

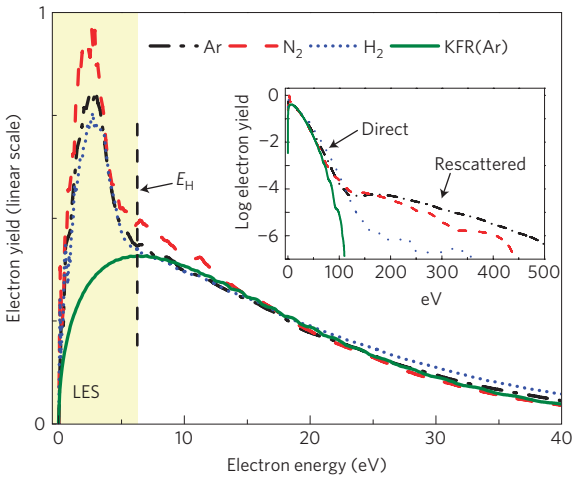

Figure 1 | Typical photoelectron energy distributions in the tunnelling regime. The low-energy region of the spectra for argon, molecular nitrogen and molecular hydrogen produced by 150 TW cm^{-2}, 2.0 μm pulses. The intensity-averaged KFR calculation using Volkov states shows a strong deviation from the measured distributions in the shaded region. The dashed line labelled E_H defines the high-energy limit of the LES used in the analysis. Inset: The entire photoelectron energy distribution exhibits the well-documented behaviour of the 'direct' and 'rescattered' electrons. The first-order KFR calculation neglects rescattering and consequently is not expected to reproduce the rescattered plateau. For comparison, the theoretical result is adjusted to match the normalized experimental distributions at 15 eV.

The high-dynamic-range experiments presented here probe the electron distributions deeper into the tunnelling regime (γ approaching 0.1) than previously reported. Consequently, the semi-classical and KFR models are expected to become more valid. The main observation reported here is at variance with this expectation: as shown in Fig. 1, a low-energy structure (LES) prominent in the experiment is conspicuously absent in the theory. As the LES is observed to become more visible with decreasing γ, the long wavelengths used in the experiments are a key element in revealing this previously undetected feature.

The experiment has been described previously[13]: the electron energy spectrum is produced by irradiating atoms or molecules by intense (10^{13}–10^{15} W cm^{-2}), ultrashort (50–120 fs), mid-infrared (0.8–3.6 μm) laser pulses. The photoelectrons are detected in a ±6° angle around the laser polarization direction by a time-of-flight spectrometer.

[1]Department of Physics, The Ohio State University, Columbus, Ohio 43210, USA, [2]Department of Physics and Astronomy, Stony Brook University, Stony Brook, New York 11794, USA, [3]Institute of Optics and Quantum Electronics, Friedrich Schiller University of Jena, 07743 Jena, Germany, [4]Department of Physics, Texas A&M University, College Station, Texas 77843, USA, [5]FOM AMOLF 407 Kruislaan, 1098 SJ Amsterdam, The Netherlands.
*e-mail: dimauro@mps.ohio-state.edu.

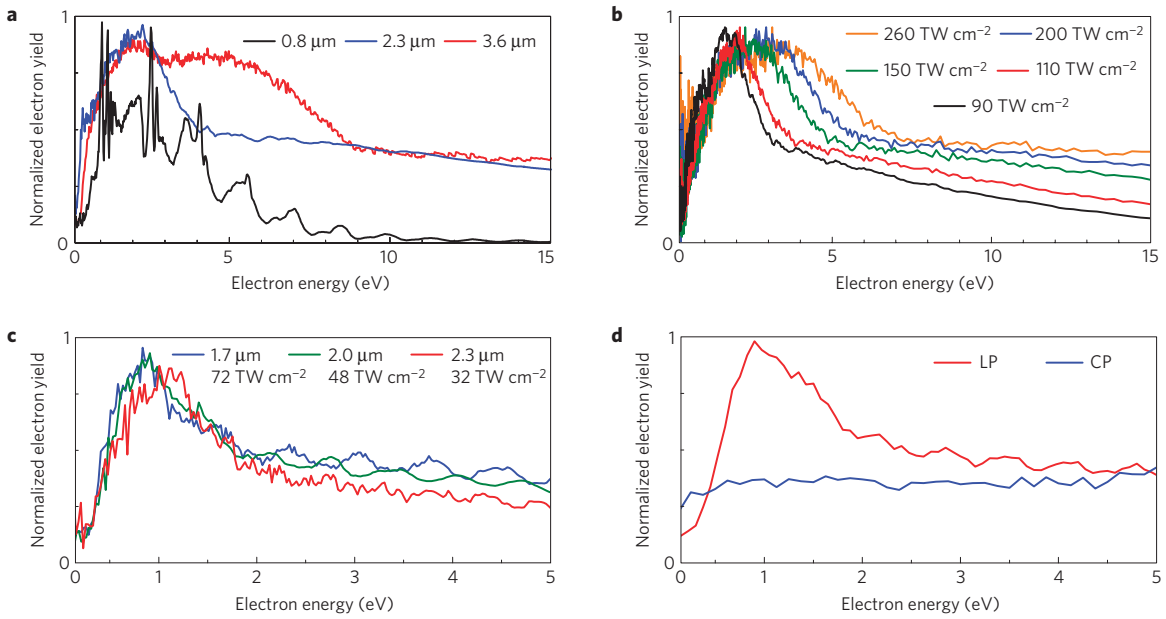

Figure 2 | Evolution of the photoelectron distributions in the LES region. a, The emergence of the LES as a function of wavelength for xenon at the saturation intensity (80 TW cm^{-2}). **b**, The progression of the LES in argon at 2.0 μm as a function of intensity. **c**, The LES in xenon for constant ponderomotive energy ($U_p \sim 19$ eV) or constant Keldysh parameter ($\gamma \sim 0.56$). **d**, The LES region in xenon for linearly (LP) and circularly (CP) polarized 2.0 μm pulses for a peak vector potential of 1.8 atomic units.

The LES spectra shown in Fig. 1 are typical of all inert gas atoms (He, Ne, Ar, Kr, Xe) and diatomic molecules (N_2, H_2, D_2) studied at long wavelength ($\lambda > 1\,\mu$m) and thus seem universal. The LES details depend on the laser characteristics and the atom/molecule under investigation but its structure can be characterized by a peak energy (1–5 eV) and high energy limit ($E_H \sim 2$–20 eV) defined by the break in slope that approximately coincides with the divergence from the semi-classical prediction. As will be discussed, a necessary condition for the appearance of this feature is $\gamma \ll 1$ or tunnel ionization. Furthermore, the LES width is much greater than the photon energy and its integrated yield can contain up to half of the electron emission. All of the above observations are valid for linear polarized excitation. Most importantly, the observation points to an obvious breakdown in our understanding.

The reason why the LES has so far eluded observation is revealed in Fig. 2a, a plot of photoelectron energy distribution for xenon atoms ionized at constant intensity (80 TW cm^{-2}) for three different wavelengths. The 0.8 μm distribution has been well documented and shows an ATI series[14] with resonant Rydberg substructure[15], characteristic of the multiphoton regime ($\gamma \geq 1$) and dynamics. However, as the wavelength increases in Fig. 2a, the LES feature becomes progressively visible and broadens in width. Excluding this low-energy portion, the remaining spectrum is consistent with the tunnelling limit and the semi-classical behaviour (see Fig. 1, inset). Consequently, the remainder of the analysis will focus on the low-energy spectral region.

Perceptive views of the LES feature are presented in Fig. 2b–d. As the intensity rises towards saturation at constant wavelength, the normalized LES distributions in Fig. 2b change in width and peak energy. In contrast, Fig. 2c shows three nearly identical xenon electron distributions recorded at a constant value of $U_p \sim 19$ eV. Remarkably, this corresponds to widely different conditions varying from 1.7 μm pulses near the saturation intensity to 2.3 μm pulses at half this intensity. Thus, the LES feature seems invariant with respect to the field parameters if U_p is constant. However, preliminary results presented in Fig. 2d show a suppression of the LES feature for circular polarization.

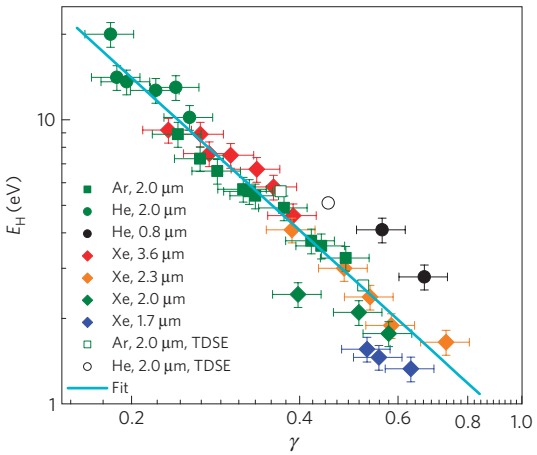

Figure 3 | LES mapping for various atoms and wavelengths. The dependence of E_H versus the Keldysh parameter (γ) for argon (filled square: experiment, open square: TDSE), helium (filled circle: experiment, open circle: TDSE) and xenon (filled diamond). The solid line is a fit to all of our LES data and suggests a simple scaling law, $E_H \simeq \gamma^{-\alpha}$ with $\alpha = 1.78 \pm 0.1$. The abscissa error bars are due to a 20% accuracy in estimating the laser intensity and the ordinate error bars account for the spectrometer calibration and the uncertainty determining the extent of the LES region.

An equivalent interpretation of the invariant condition in Fig. 2c is that γ is also fixed ($\simeq 0.56$). Moreover, the similarity of the three different LES distributions shown in Fig. 1 for Ar, H_2 and N_2 with approximately constant $\gamma \sim 0.4$ (binding energies equal within 3% and constant intensity and wavelength) supports a correlation with the Keldysh picture. To investigate this connection, Fig. 3 shows the LES high-energy limit, E_H, versus the Keldysh parameter, γ, for three different targets (He, Ar and Xe) at various wavelengths (0.8, 1.7, 2.0, 2.3 and 3.6 μm). Over the entire range, the logarithmic plot suggests the LES obeys a simple scaling law $E_H \sim \gamma^{-\alpha}$ with $\alpha \sim 1.8 \pm 0.1$. For $\gamma \leq 0.5$, deep in the tunnelling regime, the scaling

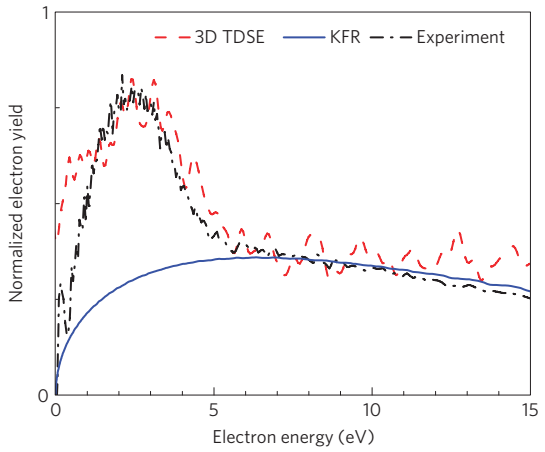

Figure 4 | Comparison of calculated and measured LES distributions for argon ionized by 150 TW cm^{-2}, 2 μm pulses. The experiment is remarkably well reproduced by the three-dimensional TDSE. For comparison, the KFR using Volkov states fails in this region. The calculated distributions are obtained using intensity averaged, 10-cycle flat-top pulses (see the Methods section).

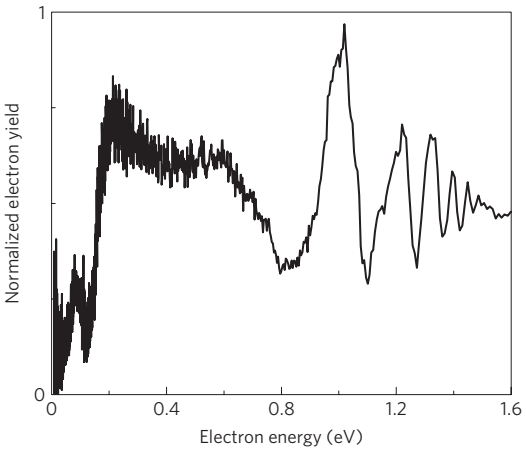

Figure 5 | The first ATI peak in argon at 120 TW cm^{-2}, 0.8 μm. The Rydberg series substructure is clearly visible in the multiphoton regime ($\gamma \simeq 1.1$). The spectrometer's low-energy roll-off occurs below 0.3 eV, whereas the LES spans the region up to 20 eV.

is excellent despite the strikingly different experimental conditions; for example, xenon at 3.6 μm scales identically with helium or argon at 2.0 μm. For $\gamma > 0.5$, the data is more scattered, probably because of the gradual passage from tunnelling to multiphoton, but the scaling is still a reasonable fit.

The above discussion establishes the existence of the LES as a feature manifested in the tunnelling regime but its origin is not obvious. Numerical solutions of the three-dimensional time-dependent Schrödinger equation (TDSE) within the single-active-electron approximation have been shown to yield essentially exact results in argon[15] or helium[16] at a wavelength of 0.8 μm. At 2 μm, the same numerical method also successfully reproduces the measured LES whereas the KFR result does not (see Fig. 4 in argon at 150 TW cm^{-2}). This provides an opportunity for theoretical deconstruction of the LES for identifying the physics present in TDSE but neglected in KFR and semi-classical approaches. First, the role of excited states is investigated because this is absent from both the KFR theory and the tunnel ansatz of the semi-classical theory. This contribution can be tested by replacing the realistic argon potential in the TDSE calculation by a modified one supporting a single bound state (argon ground level). The result is essentially unchanged; thus, the LES seems to be independent of excited state structure. Second, the Coulomb distortion of the final state is examined by using the well-known Coulomb–Volkov wavefunction in the KFR calculation[17]. Again, the LES is not reproduced, similar to the pure Volkov state. By simple deduction, this suggests that some form of rescattering is involved. Briefly, rescattering is the interaction of a field-driven continuum electron wave packet with its core after ∼(1/2)-cycle of 'free' propagation. This process is responsible for the production of both plateau electrons and high-harmonic radiation. The persistence of the LES in our TDSE numerical analysis using pulse durations down to one cycle supports the interpretation as a rescattering event, not a multi-cycle interference. The rescattering hypothesis is also consistent with the observed polarization dependence. In contradiction, rescattering also implies a reduced LES yield with increasing wavelength due to the energy-dependent elastic cross-section (the plateau electron yield drops as $1/\lambda^4$; ref. 13), whereas the measured LES has constant amplitude as long as the tunnelling condition is satisfied.

The observations reported here point to a lack of completeness in our understanding of strong-field physics. Of course, under the conditions of the experiment, it is obvious that the non-relativistic Schrödinger equation is the correct framework and indeed it seems to be numerically correct. However, the LES does not fit in the well-established picture that provides a clear classical foundation to strong-field atomic ionization. The corrections that its eventual understanding will necessarily impose on the KFR and semi-classical approaches should shed new light on this fundamental process in the tunnel limit and suggest new directions of research. Clearly, more investigations are needed to understand this effect discovered forty years after Keldysh's seminal paper. In addition, experimentalists will have another opportunity to push the limits of strong-field physics with the advent of hard X-ray free-electron lasers.

Methods

The details of the three laser systems used in these experiments can be found in ref. 13.

Electron spectrometer. The time-of-flight electron energy spectrometer was previously described[13]. Here, we provide some details on the special precautions required for the detection of the low-energy electrons of the LES as they are sensitive to stray fields and contact potentials. Efficient shielding of the time-of-flight region against both magnetic and electric external fields is achieved with gold plated, μ-metal and a graphite coating (Aerodag G) minimizes patch effects. Besides applying the usual precautions to prevent space charge effects (the target density for a given laser intensity is adjusted to limit the count rate to ≤0.5 electron per laser shot for a detection efficiency estimated to be around 1–3%), the drop of the spectrometer transmission for very low-kinetic-energy electrons must be taken into account. To establish the low-energy transmission, we studied the well-known argon ATI spectrum at 0.8 μm, presented in Fig. 5. The figure shows the well-resolved Rydberg resonance structure of the first ATI peak followed by a rapid decrease below 0.3 eV due to the electron spectrometer's transfer function. This portion is small compared with the region of interest for the LES and therefore its effect is negligible. As a large fraction of electrons is emitted within the LES, relatively short runs (10^3 s at 1 kHz repetition rate) were required to achieve good counting statistics below 3%.

Numerical simulations. The KFR theory uses the first-order Born approximation to calculate the ionization process. Within this approximation the rescattering process is neglected. In the length gauge, the transition amplitude is written as $\int \langle \Psi_V(\mathbf{k},\mathbf{r},t) \,|\, \mathbf{E}(t)\mathbf{r} \,|\, \Psi_i(\mathbf{r},t)\rangle \, \mathrm{d}t$, where $\Psi_V(\mathbf{k},\mathbf{r},t)$ is the final state, $\mathbf{E}(t)$ is the electric field and $\Psi_i(\mathbf{r},t)$ is the initial ground state. The integral over space is carried out analytically, whereas the integral over time is carried out numerically using the saddle point method[18]. We use short-range or Hartree–Fock[19] initial wavefunctions and Volkov or Coulomb–Volkov[17] final states. The Volkov state is the exact solution of the Schrödinger equation for an electric charge interacting with a laser field, whereas the Coulomb–Volkov wavefunction is an approximation to account for the interaction of a charge particle with a laser field and a Coulomb potential. This last wavefunction does not include multiple collisions but only a distortion of the wavefunction when the electron is ionized.

The TDSE method is the numerical solution of the Schrödinger equation on a spatio-temporal grid. Calculations were carried out within the single-active-electron

approximation in the velocity gauge. The numerical procedure has been described in detail elsewhere[13,20,21]. Different model potentials were used for argon and helium, as well as a Yukawa potential supporting a single bound state.

For comparison to the experimental electron distributions, all of the calculated spectra are weighted over the spatial profile of a Gaussian laser focus.

All theoretical distributions represent the quantity $(\partial W/\partial E\partial\Omega)|_{\theta=\phi=0}$, meaning the wavefunction of the photoelectron is analysed along the direction of the laser polarization.

The computational accuracy of the KFR simulation, spatially averaged, is achieved within 1%. The saddle point method accurately reproduces the discrete numerical time integration of the amplitude provided that the short-range wavefunction is used. The TDSE calculation is carried out for different grid sizes and angular momenta to assure numerical convergence of the photoelectron spectrum within 1–3%. The TDSE calculation is computationally intensive at long wavelengths and high intensities; thus, the spatial averaging is the main limitation on the accuracy. Nonetheless, the averaging is carried out such that three consecutive intensities produce a shift of the ATI peak that is less than a photon energy. This procedure assures a global convergence of the calculation within 10%.

Received 22 December 2008; accepted 19 February 2009; published online 29 March 2009

References

1. Becker, W. *et al.* Above-threshold ionization: From classical features to quantum effects. *Adv. At. Mol. Opt. Phys.* **48**, 35–98 (2002).
2. Moshammer, R. *et al.* Momentum distributions of Ne^{n+} ions created by an intense ultrashort laser pulse. *Phys. Rev. Lett.* **84**, 447–450 (2000).
3. Paulus, G. G. *et al.* Measurement of the phase of few-cycle laser pulses. *Phys. Rev. Lett.* **91**, 253004 (2003).
4. van Linden van den Heuvell, H. B. & Muller, H. G. *Multiphoton Processes* 25–34 (Cambridge Univ. Press, 1987).
5. Keldysh, L. V. Ionization in the field of a strong electromagnetic wave. *Sov. Phys. JETP* **20**, 1945–1950 (1964).
6. Faisal, F. H. Multiple absorption of laser photons by atoms. *J. Phys. B* **6**, L89–L92 (1973).
7. Reiss, H. R. Effect of an intense electromagnetic field on a weakly bound system. *Phys. Rev. A* **22**, 1786–1813 (1980).
8. Paulus, G. G., Nicklich, W., Huale, Xu, Lambropoulos, P. & Walther, H. Plateau in above-threshold ionization spectra. *Phys. Rev. Lett.* **72**, 2851–2854 (1994).
9. Yang, B. *et al.* Intensity dependent rings in high-order ATI. *Phys. Rev. Lett.* **71**, 3770–3773 (1993).
10. Walker, B., Sheehy, B., Kulander, K. C. & DiMauro, L. F. Elastic rescattering in the strong field tunneling limit. *Phys. Rev. Lett.* **77**, 5031–5034 (1996).
11. Ray, D. *et al.* Large-angle electron diffraction structure in laser-induced rescattering from rare gases. *Phys. Rev. Lett.* **100**, 143002 (2008).
12. Morishita, T., Le, A-T., Chen, Z. & Lin, C. D. Accurate retrieval of structural information from laser-induced photoelectron and high-order harmonic spectra by few-cycle laser pulses. *Phys. Rev. Lett.* **100**, 013903 (2008).
13. Colosimo, P. *et al.* Scaling strong-field interactions towards the classical limit. *Nature Phys.* **4**, 387–389 (2008).
14. Agostini, P., Fabre, F., Mainfray, G., Petite, G. & Rahman, N. K. Free-free transitions following six-photon ionization of xenon atoms. *Phys. Rev. Lett.* **42**, 1127–1130 (1979).
15. Nandor, M. J., Walker, M. A., Van Woerkom, L. D. & Muller, H. G. Detailed comparison of above-threshold-ionization spectra from accurate numerical integrations and high-resolution measurements. *Phys. Rev. A* **60**, R1771–R1774 (1999).
16. Muller, H. G. Tunneling excitation to resonant states in helium as main source of superponderomotive photoelectrons in the tunneling regime. *Phys. Rev. Lett.* **83**, 3158–3161 (1999).
17. Duchateau, G., Cormier, E., Bachau, H. & Gayet, R. Coulomb–Volkov approach of atom ionization by intense and ultrashort laser pulses. *Phys. Rev. A* **63**, 053411 (2001).
18. Miloševiç, D. B., Paulus, G. G., Bauer, D. & Becker, W. Above-threshold ionization by few-cycle pulses. *J. Phys. B* **39**, R203–R262 (2006).
19. Byron, F. W. Jr. & Joachain, C. J. Correlation effects in atoms. I. Helium. *Phys. Rev.* **146**, 1–8 (1966).
20. Tate, J. *et al.* Scaling of wave-packet dynamics in an intense midinfrared field. *Phys. Rev. Lett.* **98**, 013901 (2007).
21. Muller, H. G. & Kooiman, F. C. Bunching and focusing of tunneling wave packets in enhancement of high-order above-threshold ionization. *Phys. Rev. Lett.* **81**, 1207–1210 (1998).

Acknowledgements

This work was carried out with support from the National Science Foundation under contract PHY-0653022. L.F.D. acknowledges support from the Hagenlocker chair. G.G.P. acknowledges support by the AFOSR.

Additional information

Reprints and permissions information is available online at http://npg.nature.com/reprintsandpermissions. Correspondence and requests for materials should be addressed to L.F.D.